Time-Resolved Photoimaging of Image-Potential States in Carbon Nanotubes

M. Zamkov, N. Woody, B. Shan, H. S. Chakraborty, Z. Chang, U. Thumm, and P. Richard

James R. Macdonald Laboratory, Department of Physics, Kansas State University, Manhattan, Kansas 66506-2604, USA

The first experimental evidence for the existence of image-potential states in carbon nanotubes is presented. The observed features constitute a new class of surface image states due to their quantized centrifugal motion. Measurements of binding energies and the temporal evolution of image state electrons were performed using femtosecond time-resolved photoemission. The associated lifetimes are found to be significantly longer than those of $n = 1$ image state on graphite, indicating a substantial difference in electron decay dynamics between tubular and planar graphene sheets.

PACS numbers: 73.21.–b, 73.22.–f, 73.90.+f

Quantized states are known to form in front of surfaces due to the polarizing image-interaction of an external electron. For years, the investigation of these states above metal surfaces has served as a powerful tool for probing a variety of physical and chemical phenomena on the nanometer scale [1–10]. The unique properties of image states are determined by the extreme sensitivity of ''image'' electrons to any changes in the dielectric susceptibility at the surface. Therefore, through measurements of their binding energies and lifetimes it is possible to elucidate many complex processes that ultimately promote our knowledge of surface structure, optical properties at interfaces [7], electronic structure at heterojunctions [8], layer growth morphology [9], and surface reactivity [10].

Following their first observation [11], the experimental exploration of image-potential states was limited, almost exclusively, to metal surfaces [1,3,4]. However, the whole arsenal of spectroscopic tools for probing metallic image states can be applied to systems, which are at the core of nanomaterial and nanodevice research. Indeed, the observation of image states in a variety of nanoscopic settings including molecular nanowires [12], metal nanoclusters [13], and even liquid He [14,15] has become possible. In this context, the study of image-potential states in carbon nanotubes is of unique interest. The cylindrical geometry of the nanotube induces a special rotational degree of freedom, which gives rise to a centrifugal force that counters the electron's association with the bulk. For a strong centrifugal repulsion associated with high values of electron angular momenta, single wall carbon nanotubes (SWNT) were predicted to support the *tubular* image states that form in the potential well between the repulsive barrier and the long-range image-interaction [16]. On the other hand, our recent study [17] has suggested that in addition to tubular image states, both single and multiwalled carbon nanotubes can support low- and zero-angular momentum image states with weak transverse penetrations into the bulk (see Fig. 1). We argued that in sharp contrast to image states above metal surfaces, where the conduction band-embedded delocalization of a state is also possible, the image-potential state of

a nanotube can always be localized, and hence experimentally accessible, due to the electron's reflection from the transverse potential wall inside the carbon cage. This universal availability of nanotube image states for localized excitations and their augmented sensitivity to the surface structure make them strong candidates for surface spectroscopic and STM [18] studies.

Here, we report the first experimental evidence of image-potential states in carbon nanotubes. The observed features constitute a new class of surface image states owing to their quantized centrifugal motion. Measurements of binding energies and the temporal evolution of image state electrons were performed using femtosecond time-resolved photoemission. The associated image electron lifetimes are found to be significantly longer than those of $n = 1$ image state on graphite [19], indicating a substantial difference in electron decay dynamics between tubular and planar graphene sheets.

The appearance of individual nanotubes within a sample plays a key role in the formation of image-potential
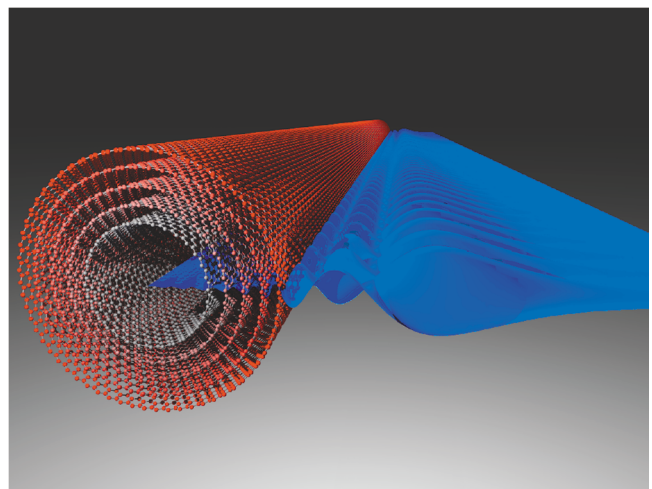

FIG. 1 (color). Visualization of an image electron wave function, $\psi_{n=3,l=1}(\rho)e^{ikz}$ calculated for a 5 nm MWNT. The angular component of the wave function, $e^{il\phi}$, [see Eq. (1)] is set to unity.

0031-9007/04/93(15)/156803(4)$22.50　　　© 2004 The American Physical Society

states. Because of the fact that image electrons are spatially extended from the tube's surface at distances of up to a few nanometers [16], the nanotubes need to be isolated from any source of interaction, such as the substrate or other SWNTs. Synthesis of the adequate size SWNT sample with the latter characteristics is complicated by the tendency of SWNTs to form bundles (ropes) [20]. Thus, as a viable alternative, samples of individual multi walled carbon nanotubes (MWNT), are used in the present study [21]. The diameter distribution of high-purity (>95%) MWNTs was within 10–20 nm, as confirmed by STM measurements. The samples used in the photoemission study consisted of 0.4-mm-thick freestanding MWNT "buckypaper," which was attached to a Ta substrate and outgassed thoroughly in multiple heating and annealing cycles with a peak temperature of 700 K.

Energetics of the two-photon photoemission is presented in Fig. 2(a). Initially, the UV pump-photon with an energy of 4.71 eV photoexcites an electron out of an occupied state below the Fermi level, E_F, into an image-potential state. A second fundamental frequency photon with an energy of 1.57 eV promotes the image electron to an energy above the vacuum level, E_{vac}, and its resulting kinetic energy is measured.

The experimental setup consisted of a Ti:sapphire laser system generating 35 femtosecond pulses at 2 kHz. Frequency-tripled UV photons were produced through

nonlinear effects during the photoionization of N_2 molecules. The fluence of the resulting 100 fs UV pump-pulse used for promoting an electron population into unoccupied image states was estimated to be 40 μJ/cm^2. Binding energies and temporal dynamics of photoexcited electrons were subsequently probed with a delayed IR probe-pulse having a fluence of 30 μJ/cm^2. The single-photon ionization regime, critical for the correct interpretation of the photoelectron energy distribution, was established by requiring that the photoemission signal is independent of the polarization of the IR probe-beam. In order to increase the count rate to pulse fluence ratio, the laser spot size on the sample for both UV and IR beams was maintained relatively large (~400 μm). Following the photoionization by IR pulses, electrons drifted into the magnetically and electrically shielded 30-cm long spectrometer tube and were detected with a strip-and-wedge position sensitive detector. The overall energy resolution of the system in the case of 1 eV electrons was 20 meV.

In the present study, the energy of the UV photon exceeded the sample work function of 4.24 ± 0.10 eV by 0.47 eV, resulting in a pump-only photoemission of low-energy electrons. In order to isolate the photoemission originating from image-potential states, we recorded the change in the photoelectron signal induced by the IR probe-pulse. This approach is illustrated in Fig. 2(c) showing the two photoelectron spectra, resulting from "pump-only" and "pump and probe" photoemission. The corresponding "excitation" difference is shown in Fig. 2(b). For a negative pump-probe delay, the IR pulse is incident first, promoting the electron population from below the Fermi level into the conduction band. The resulting perturbation, consisting of $\bar{e}$–h pairs, is then probed with a UV pulse, giving rise to a characteristic feature [22] in the photoelectron spectrum (the bipolar peak in 2(b)]. This signal fades for a positive pump-probe delay of approximately 150 fs (the convoluted duration of UV and IR pulses), since the amount of UV photons, following the IR pulse and, thus, probing excited carriers at the Fermi level is now negligibly small. For delays exceeding 200 fs, most of the photoelectrons are created with a single IR probe-photon. The corresponding window of accessible electronic states for this configuration is located within 1.57 eV below the vacuum level [see Fig. 3(a)], which is degenerate with the expected positions of image-potential states as well as the continuum of states at the top of the conduction band. The excited electron population in the latter has a characteristic lifetime of just a few femtoseconds [23]. Meanwhile, the photoelectron signal is still observed for pump-probe delays of up to 0.5 ps (see Fig. 3). Therefore, the observed photoemission, shown in Fig. 2(b), is attributed to the photoionization of image-potential states in MWNTs.

In order to link the experimental data with theoretical expectations, we have developed a comprehensive model
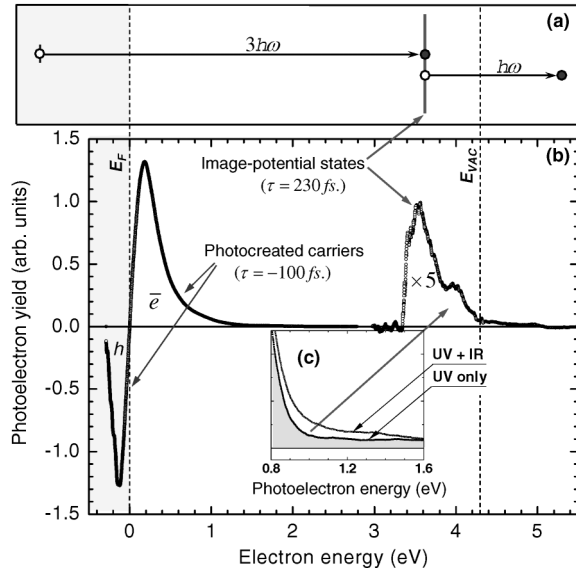

FIG. 2. (a) The energy diagram of a two-photon photoexcitation technique. (b) The experimental photoelectron signal is plotted versus the electron energy relative to the Fermi level. If the IR pulse precedes the UV pulse ($\tau = -100$ fs), $\bar{e}$–h pairs (excitons) are created in the vicinity of E_F (taken as zero of the energy scale). Image-potential states are observed just below the vacuum level for a positive delay of 230 fs. (c) The insert shows the change in the UV photoelectron signal induced by the IR probe-pulse.
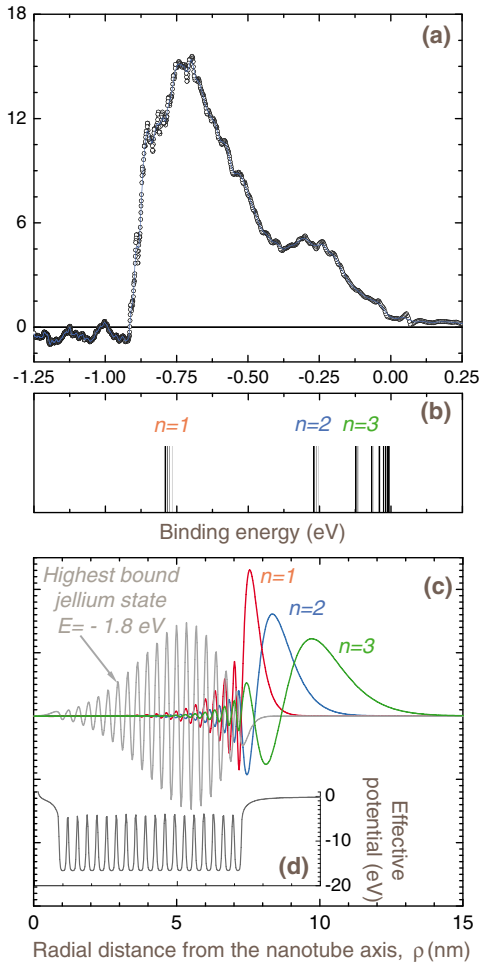
FIG. 3 (color).   (a) The photoelectron signal, originating from image-potential states, is plotted versus electron binding energies. Theoretical calculations of binding energies (b) and the associated wave functions, $\psi_{n,l}(\rho)$, (c) were performed for a 19-walled carbon nanotube ($d = 14.2$ nm). The model utilizes the jelliumlike potential barrier [17,26], shown in (d). Different shades of energy bars in (b) represent different electron angular momenta ($0 \le l \le 4$).

describing an image-potential state of a MWNT. First, owing to the cylindrical symmetry of the system, the image electron motion along the nanotube's axis can be separated as:

$$\Psi_{n,l,k}(\rho, \phi, z) = \frac{1}{\sqrt{2\pi\rho}} \psi_{n,l}(\rho) e^{il\phi} e^{ikz}, \qquad (1)$$

where l is the angular momentum of an electron. The resulting one-dimensional Schrödinger equation is solved to obtain the binding energies, $E_{n,l}$, and the wave functions, $\psi_{n,l}(\rho)$, for the electron motion in the transverse direction, ρ. Effective interactions of an image electron with the surface of a nanotube are modeled by introducing a cylindrical jelliumlike potential barrier [17,24], parameterized to ensure the correct transition into the long-range image-potential [16,25] at the tube-vacuum

interface. Figure 3(d) shows the total effective potential calculated for a 19-walled carbon nanotube with the outer diameter of 14.2 nm and the intertube separation of 0.34 nm. The associated wave functions for $n = 1, 2, 3$ ($l = 1$) image-potential states are displayed in Fig. 3(c). For the classification of states, we adopt a scheme, which is similar to that of image states in metals, such that the most deeply bound state, localized on the vacuum side, is labeled as $n = 1$. The difference in the localization character between image-potential states and electronic states forming below the surface of the nanotube is seen in Fig. 3(c), where the highest bound bulk state is plotted. The corresponding binding energies of low-angular momentum ($l \le 4$) states, calculated for a 14.2-nm-diameter MWNT, are shown in Fig. 3(b).

For large-diameter nanotubes, the centrifugal repulsion of image electrons becomes less significant. Thus, binding energies of image-potential states in MWNTs are not expected to exhibit a strong dependence on the angular momentum [see Fig. 3(b)]. In addition, formation of the tubular image states [16] on the vacuum side of the centrifugal barrier will be suppressed. This claim is supported by the absence of any pronounced features in the vicinity of the vacuum level in the observed photoelectron signal, shown in Fig. 3(a). The experimental range of binding energies, on the other hand, is in excellent agreement with model predictions. Through comparison with the theoretical spectrum in Fig. 3(b), a cluster of image-potential states with $n = 1$ can be distinguished in the observed photoemission. Similarly, the low-energy side of the experimental spectrum, -0.3 eV $< E < 0$, can be attributed to image electrons with the higher values of principal quantum number $n = 2, 3, \ldots$.

The long-range character of the nanotube image-potential can be asymptotically expressed as [16] $1/[(\rho/a) \ln(\rho/a)]$, where a is the nanotube radius. Since this potential cannot be scaled for different values of a, positions of image-potential states below the vacuum level are expected to reflect even minor changes in the nanotube diameter. The variety of different MWNT sizes in the investigated sample, therefore, should result in the superposition of image electron energies in the photoelectron spectrum. The corresponding broadening can be seen clearly in Fig. 3(a).

We expect that electrons in image-potential states will experience the full translational symmetry for a motion parallel to the tube's axis. Consequently, their lifetimes will provide a measure of the coupling to nanotube phonons, holes, and defects. In Fig. 4, we present the time-domain measurements of the electron dynamics in image-potential states. The pump-probe delay of at least 200 fs is used to minimize the possible photoemission from electronic states created by the time-reversed pair of IR and UV photons. The total electron signal, integrated
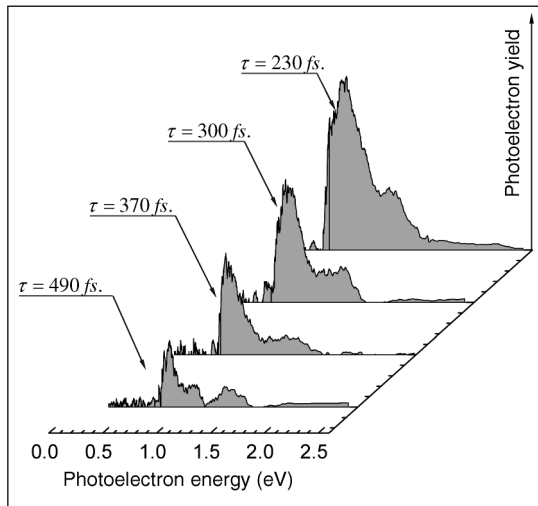
FIG. 4. The temporal evolution of the $\psi_{n=1,l}$ image-potential state. The minimum pump-probe delay of 200 fs is used to avoid the background photoemission, generated by the time-reversed pair of laser pulses (IR followed by UV). The energy scale represents the kinetic energy of photoelectrons emitted from image-potential states by the IR probe-pulse.

over the binding energy in the vicinity of the $n = 1$ state, fits the monoexponential decay curve with a time constant of 220 ± 5 fs. The latter is substantially longer than the 40 fs lifetime of the $n = 1$ image state on graphite surface. The resulting elongation of the electronic lifetimes in MWNTs that can be viewed as coaxial tubules of graphene sheets is likely the effect of a combination of factors (localization, geometry, screening, and defects), of which no single one can be identified in the present experiment. However, in a single-electron formalism, the longer lifetimes of nanotube image-potential states were attributed to a weaker coupling of image state wave functions to bulk, resulting from the localization and cylindrical geometry [17].

In conclusion, we present experimental evidence for the existence of image-potential states in carbon nanotubes. These states provide a novel setting for the investigation of nanotube surface phenomena, including surface reactivity and growth kinetics, structural and optical properties at interfaces, electronic transport in nanotube heterojunctions, and adsorbate reactions. It is expected that similar states can also be created in single walled nanotubes as well as in nanotube bundles, opening new avenues in the investigation of these nanostructures.

[1] U. Höfer et al., Science **277**, 1480 (1997).
[2] T. Hertel, E. Knoesel, M. Wolf, and G. Ertl, Phys. Rev. Lett. **76**, 535 (1996).
[3] A. D. Miller et al., Science **297**, 1163 (2002).
[4] W. Berthold et al., Phys. Rev. Lett. **88**, 56805 (2002).
[5] D. C. Marinica et al., Phys. Rev. Lett. **89**, 046802 (2002).
[6] D. F. Padowitz, W. R. Merry, R. E. Jordan, and C. B. Harris, Phys. Rev. Lett. **69**, 3583 (1992).
[7] R. L. Lingle et al., Phys. Rev. Lett. **72**, 2243 (1994).
[8] T. Schmitz-Hübsch, K. Oster, J. Radnik, and K. Wandelt, Phys. Rev. Lett. **74**, 2595 (1995); P. D. Loly and J. B. Pendry, J. Phys. C **16**, 423 (1983).
[9] R. Fischer, Th. Fauster, and W. Steinmann, Phys. Rev. B **48**, 15496 (1993).
[10] N. Memmel and E. Bertel, Phys. Rev. Lett. **75**, 485 (1995).
[11] P. D. Johnson and N. V. Smith, Phys. Rev. B **27**, 2527 (1983).
[12] I. G. Hill and A. B. McLean, Phys. Rev. Lett. **82**, 2155 (1999); J. E. Ortega, F. J. Himpsel, R. Haight, and D. R. Peale, Phys. Rev. B **49**, 13859 (1994).
[13] V. Kasperovich, K. Wong, G. Tikhonov, and V. V. Kresin, Phys. Rev. Lett. **85**, 2729 (2000).
[14] P. M. Platzman and M. I. Dykman, Science **284**, 1967 (1999); C. C. Grimes and T. R. Brown, Phys. Rev. Lett. **32**, 280 (1974).
[15] P. Glasson et al., Phys. Rev. Lett. **87**, 176802 (2001).
[16] B. E. Granger, P. Kral, H. R. Sadeghpour, and M. Shapiro, Phys. Rev. Lett. **89**, 135506 (2002).
[17] M. Zamkov et al., Phys. Rev. B **70**, 115419 (2004).
[18] P. Wahl et al., Phys. Rev. Lett. **91**, 106802 (2003).
[19] J. Lehmann et al., Phys. Rev. B **60**, 17037 (1999).
[20] J. Liu et al., Science **280**, 1253 (1998).
[21] NanoLab, Inc., 55 Chapel Street Newton, MA 02458, USA
[22] T. Hertel and G. Moos, Phys. Rev. Lett. **84**, 5002 (2000).
[23] T. Hertel, R. Fasel, and G. Moos, Appl. Phys. A **75**, 449 (2002).
[24] P. J. Jennings, R. O. Jones, and H. Weinert, Phys. Rev. B **37**, 6113 (1988).
[25] N. R. Arista and M. A. Fuentes, Phys. Rev. B **63**, 165401 (2001).
[26] U. Thumm, P. Kürpick, and U. Wille, Phys. Rev. B **61**, 3067 (2000).